# Probing the Band Structure of Topological Silicon Photonic Lattices in the Visible Spectrum

Siying Peng (彭斯颖),[1] Nick J. Schilder,[2] Xiang Ni,[3,6] Jorik van de Groep,[4] Mark L. Brongersma,[4] Andrea Alù,[3,5,6] Alexander B. Khanikaev,[3,6] Harry A. Atwater,[1] and Albert Polman[2,*]

[1]*Applied Physics, California Institute of Technology Pasadena, California 91125, USA*
[2]*Center for Nanophotonics, AMOLF, Science Park 104, 1098 XG, Amsterdam, Netherlands*
[3]*Department of Electrical Engineering, City College of City University of New York, New York 10031, USA*
[4]*Geballe Laboratory for Advanced Materials, Stanford University, 476 Lomita Mall, Stanford, California 94305, USA*
[5]*Photonics Initiative, Advanced Science Research Center, City University of New York,*
*85 St. Nicholas Terrace, New York, New York 10031, USA*
[6]*Physics Program, The Graduate Center, City University of New York, 365 Fifth Avenue, New York, New York 10016, USA*

We study two-dimensional hexagonal photonic lattices of silicon Mie resonators with a topological optical band structure in the visible spectral range. We use 30 keV electrons focused to nanoscale spots to map the local optical density of states in topological photonic lattices with deeply subwavelength resolution. By slightly shrinking or expanding the unit cell, we form hexagonal superstructures and observe the opening of a band gap and a splitting of the double-degenerate Dirac cones, which correspond to topologically trivial and nontrivial phases. Optical transmission spectroscopy shows evidence of topological edge states at the domain walls between topological and trivial lattices.

Topological photonic materials guide light in unconventional ways, enabling entirely new ways to route information for communication and computing purposes [1–3]. Topological phases of light supported by well-designed nanostructures have the unique property that backscattering induced by imperfections is topologically forbidden, allowing lossless photon transport in large-scale optical integrated circuits. Experimentally, topological properties of light have been studied in various systems, such as one-dimensional gratings [4], two-dimensional lattices [5–8], and three-dimensional photonic crystals [9]. Using spectroscopic techniques at microwave frequencies, photonic band structures and edge modes were mapped out and proven to be topological [6,9]. In the infrared spectral range, coupled ring resonators with artificially induced magnetic fields show topological protection of edge states from defects [8] and spontaneous emission from chiral quantum dot states was shown to be guided unidirectionally in a topological silicon photonic crystal structure [10]. In the visible spectral range, three-dimensional Floquet topological insulators were demonstrated using evanescently coupled chiral waveguide elements arranged in a two-dimensional geometry [7]. For this purpose, relatively large optical elements ($> 4 \mu m$) were used, spaced at a distance of 15 $\mu m$.

However, to date there has been no experimental demonstration of topological photonic crystals that operate in the visible spectral range, and that employ nanoscale architectures compatible with planar silicon device integration. Recent research has focused on tailoring lateral lattice symmetry to create topological protection, creating a way to drastically shrink the volume necessary for the optical elements. For example, topological protection was theoretically shown by breaking the inversion symmetry of a hexagonal lattice, by splitting the degeneracy of valley degrees of freedom [11].

Another elegant and practical geometry, recently proposed theoretically, creates topological protection via pseudo-time-reversal symmetry by rearranging the elements of a two-dimensional hexagonal lattice while preserving its $C_6$ symmetry [12,13]. By expanding or shrinking the unit cells to create a hexagonal superstructure, a band gap opens in the Dirac-type band structure for TM waves, with harmonic photonic modes representing electronic orbital-like $p$- and $d$-type waves. Here, we experimentally realize these lattices composed of nanoscale silicon Mie resonators. By tailoring their geometry at the nanoscale, locally shrinking or expanding the unit cell, we create geometries in which a band gap opens at the Dirac point, with controlled topological properties. The two-dimensional hexagonal photonic lattice forms a unique platform to exploit the properties of topological states of light, as it enables direct measurements of the optical density of states and photonic band structure by accessing the third dimension [14]. Here, we use cathodoluminescence spectroscopy using a tightly focused electron beam as a probe for topological lattices.

Fabrication of two-dimensional hexagonal lattices operating in the visible spectral range is challenging because of

the high sensitivity of the optical band structure to nanoscale lattice imperfections. Our photonic lattice geometries are made on an ultrathin $Si_3N_4$ membrane, to create a nearly symmetric optical environment to study the topological properties. To realize this, we first lifted off a 200-nm-thick Si film by chemical etching from a silicon-on-insulator wafer, and then transferred it onto a 10-nm thick $Si_3N_4$ membrane that was spanned inside a Si hold wafer. Electron beam lithography and reactive ion etching was then used to fabricate hexagonal lattices of hexagonally shaped Si cylinders (incircle diameter 250 nm, height 130 nm) with a lattice constant of 450 nm. Full details of the fabrication process are described in the Supplemental Material [15], which includes Refs. [16–18]. Figures 1(a), 1(c), and 1(d) show a schematic of the fabricated geometry and scanning electron microscopy (SEM) images of the fabricated structures.
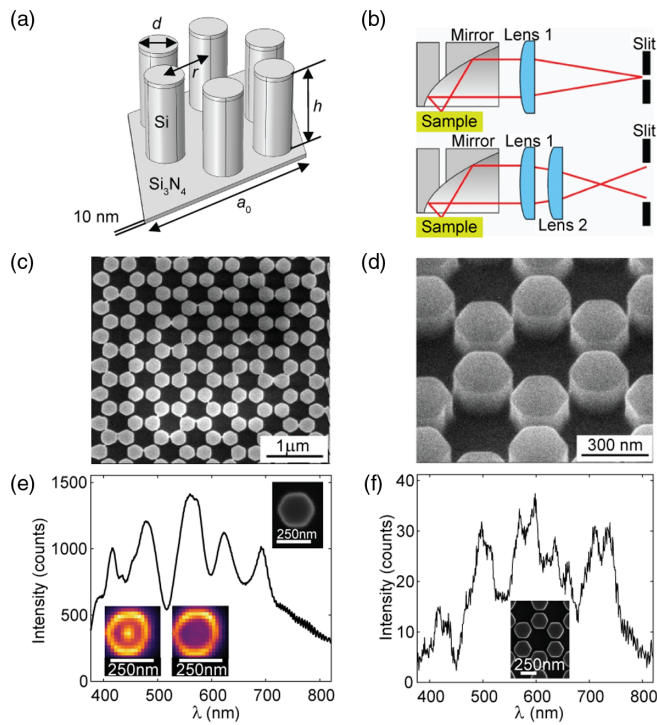


FIG. 1. Hexagonal photonic lattice and CL measurements. (a) Schematic of unit cell of expanded and shrunken lattices composed of Si hexagons composed of Si pillars on a 10-nm-thick $Si_3N_4$ membrane, where $a_0$ is the lattice constant, $d$ is the diameter of the Si pillars, $h$ is the pillar height, and $r$ is the distance of the Si pillars from the center of the unit cell. (b) Excitation geometries: the 30 keV electron beam is incident through the hole in the parabolic mirror and light emitted by the excited lattice is collected by a parabolic mirror; (top) spectral detection using a spectrometer, (bottom) angle-resolved detection using a CCD imaging camera. (c),(d) SEM images of the fabricated lattice. (e), (f) Cathodoluminescence spectra averaged over a single Mie scatterer (left, with measured mode profiles at the two most intense peaks shown as insets) and averaged over a single Mie scatterer in a hexagonal lattice (right, with inset of geometry).

To probe the photonic lattice modes at deeply subwavelength spatial resolution, we use angle-resolved cathodoluminescence imaging spectroscopy (ARCIS) using 30 keV electrons as an excitation source [19]. The time-varying evanescent field carried by the swift ($v \approx 0.3c$) electron as it traverse the sample contains a broad spectral range from the UV to the near-infrared that couples coherently to the photonic lattice modes [20]. The electron beam is raster-scanned over the lattice and the emitted light (cathodoluminescence, CL) is collected at every pixel. In contrast to the case of incoherent CL of fluorescent samples, in this coherent excitation mode there is a well-defined phase relation between the generated modal field and the electric field carried by the incident electron. The strongly localized character of the electron-induced polarization density allows probing the $z$ component of the local density of optical states (LDOS) inside the photonic lattices at a spatial resolution of 10 nm at 30 keV [21,22]. We also measure the CL emission as a function of azimuth and zenith angles in well-defined spectral bands, probing the in-plane wave vectors and thereby the photonic band structure [2]. Hyperspectral angle-resolved CL, combining spectral measurements and angle-resolved measurements along the zenithal angular range was also performed [23]. A schematic of the CL excitation geometry is shown in Fig. 1(b). In some angle-resolved measurements the sample was tilted by 7.5° to enable collection of radiation normal to the sample ($k = 0$), which is otherwise not possible because of the hole in the parabolic mirror.

Figure 1(e) shows a CL spectrum taken by averaging over a single Si cylinder (not arranged in a photonic lattice). A large number of Mie resonances is observed, consisting of in-plane and out-of-plane electric and magnetic dipolar and quadrupolar modes of the single Si cylinder, whose coherent superposition is collected in the far field [24–26]. The measured field intensities for the modes corresponding to the two most intense resonant peaks, shown as insets, reveal two characteristically different modal profiles. By tuning the coupling between neighboring scatterers, photonic lattice mode degeneracies can be controlled, leading to photonic band inversion and topologically nontrivial dispersion. As a first signature of this interaction, Fig. 1(f) shows the CL spectrum for the hexagonal lattice, with most of the resonant modes split up, characteristic for coupled resonators [27]. In order to probe the radiative local density of states inside the photonic lattice, spatial CL maps were retrieved at 426, 664, and 750 nm [Fig. 2(a)]. Comparing the maps at 664 and 750 nm, a distinct difference in the modal profiles can be observed: at 664 nm a field minimum is observed between the facing hexagon edges, while a maximum is observed at 750 nm. These features represent bonding and antibonding-type modes within the two coupled Mie resonances [23]. Such coupling is not clearly observed for the 426 nm resonance, for which the fields are more localized inside the particle.

Angle-resolved CL spectroscopy was used to characterize the dispersion of the collective photonic modes in momentum
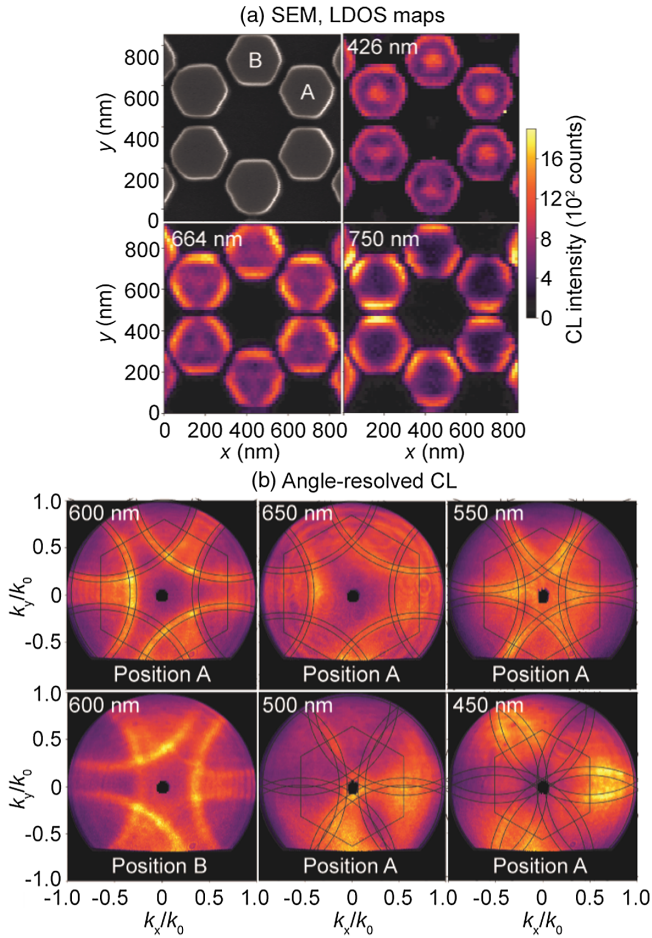
FIG. 2. Measured density of states and dispersion of hexagonal photonic lattice. (a) SEM image and CL maps at 426, 664, and 750 nm (bandwidth 10 nm). (b) Angular CL emission distributions $(k_\perp/k_0)$ for positions A in the SEM image at 650, 600, 550, 500, and 450 nm, and for position B at 600 nm, where $k_\perp$ is the in-plane wave vector and $k_0 = \omega/c$ ($k = 0$ directed towards mirror hole). The spacing between the overlaid concentric contours represents the measurement bandwidth of 40 nm. The black spots in the center correspond to the 600 $\mu$m-diameter hole in the parabolic mirror that spans 6.9° and where no light is collected.

$$E(\hat{k}) = \frac{e^{ikR}}{R} S(\hat{k}) \sum_{n=1}^{N} A_n e^{-ikr_n}, \qquad (1)$$

with $S(\hat{k})$ the form factor for an individual Mie resonator, $r_n$ is the position of individual Mie resonator, and $A_n$ the structure factor. The angular scattering distributions become narrower for increasing wavelength due to the increased propagation distance in the photonic lattice which we ascribe to the fact that silicon is less absorbing and scattering is less pronounced at larger wavelengths, which effectively increases the number of scatterers contributing to the lattice sum. The band structure derived from these data is shown in Fig. S2 [15], and shows good agreement with full-wave simulations showing near-linear dispersive bands with a Dirac point at 450 nm. See Supplemental Material [15] for a brief description of how numerical simulations were performed, which includes Ref. [29].

Next, we induce topological band splitting by shrinking $(a_0/r = 3.3)$ and expanding $(a_0/r = 2.7)$ the hexamer unit cell, while preserving $C_6$ symmetry, using Si nanopillars with $d = 88$ (lowest-order Mie resonance $\lambda \sim 470$ nm), $h = 200$, and $a_0 = 455$ nm [12]. The shrunk and expanded lattices form a hexagonal superlattice with each individual lattice site (supercell) composed of a hexamer consisting of six Si cylinders. The corresponding SEM images are shown in Fig. 3(a), together with the Brillouin zone of the basic lattice symmetry (dashed line) together with the folded Brillouin zone of the supercell lattice (solid line). Hyperspectral angle-resolved CL measurements were performed along the $\Gamma$-$K$ and $\Gamma$-$M$ directions to record angular profiles with high spectral resolution (0.87 nm) for the shrunk and expanded lattices [Figs. 3(b), 3(c)]. The sample was mounted on a 7.5° tilted sample holder, so that radiation emitted along the $\Gamma$ point could be collected (see Supplemental Material [15]). The corresponding numerical simulations of the band structures are also shown in Figs. 3(b), 3(c).

Many interesting features can be observed in Fig. 3. Theory shows that, for the shrunk lattice, inter-lattice-site coupling is enhanced, causing the Dirac cones to separate and leading to a band gap. Such band separation is clearly observed in Fig. 3(b). For the expanded lattice, intra-lattice-site coupling is enhanced, introducing band hybridization to open the band gap. The band gap for the shrunk lattice, derived from a parabolic fit near the $\Gamma$ point is 9 nm (30 meV) and for the expanded lattice is 6 nm (20 meV) [12]. For the expanded lattice, theory shows band hybridization that introduces winding of the band (pseudospin Chern number $= \pm 1$), and therefore the band gap of the expanded lattice is topologically nontrivial [12]. The two originally doubly degenerate Dirac cones each split in two pairs of bands, as also clearly observed in the CL data. For the $\Gamma$-$K$ direction the bands are closely spaced for large wave vectors, as seen in both simulations and experiment. For the $\Gamma$-$M$ direction a much larger separation between the

space [Fig. 2(b)], where the localized nature of our source allows selective addressing of different sublattices. Threefold symmetric bands are observed, rotated 60° between the two nonequivalent lattice sites in the unit cell, as expected. In-plane wave vectors $k_{wg}$ were retrieved from spherical contours fitted to the angular profiles, assuming that the angular emission is the result of diffractive outcoupling of the in-plane guided modes by the periodically arranged resonant Mie scatterers [28]. Indeed, the excitation and outcoupling of guided modes make angle-resolved CL ideally suited to probe the band structure of an extended structure like the topological photonic crystals under consideration, despite the use of a localized source. The angular distribution of the scattered light is given by a coherent sum of all scattering fields at a distance $R$:
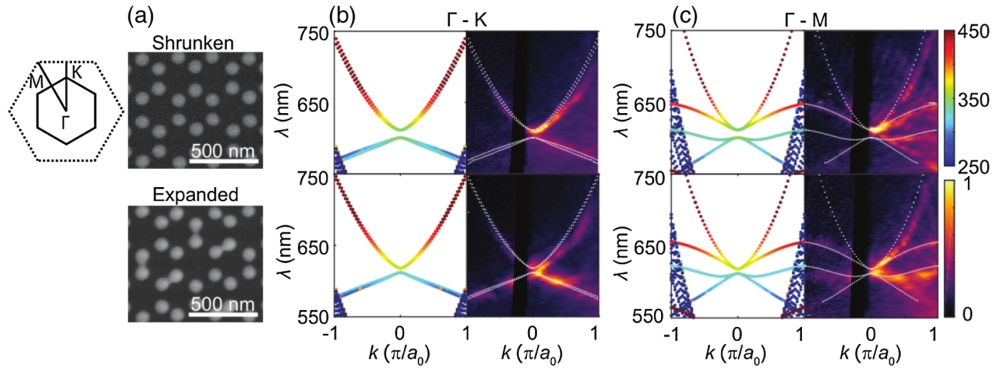
FIG. 3. Measured and simulated photonic band structure of trivial and topological lattices. (Top) shrunk lattice; bottom: expanded lattice. SEM images (a) and calculated and measured dispersion of the triangular lattice with six silicon pillars for the unit cell, along $\Gamma$-$K$ (b) and $\Gamma$-$M$ (c) directions (calculated dispersion overlaid over the measurements as dashed curves). The blue cones on either side of the calculated band structures correspond to modes outside the light cone. Data are taken with the tilted sample holder. The black vertical band in the CL data corresponds to the angular range of the hole in the parabolic mirror, where no data are collected. For the band structures, quality factor was encoded into the color of the bands.

separated bands is observed both experimentally and in simulations. Deviations of the parabolic band curvatures between theory and experiment are attributed to slight differences in the fabricated and modelled geometry.

As the topological modes at $k = 0$ exhibit flat dispersion, corresponding to zero group velocity, they are best described by their quality factor $Q$. We find the radiative $Q$ of the modes varies from $\sim$100 (for bright dipolar modes at oblique incidence) to very large numbers (for dark quadrupolar modes at normal incidence), since radiation loss is absent in this latter case [14]. From the observed broadening of the lines, we estimate that absorption and scattering in the samples leads to a reduction of the quality factor to $Q_{\text{total}} \sim 65$, implying a lifetime reduction of 35% for bright modes. Further modeling will reveal if absorption or scattering is the dominant loss process.

By creating an interface between the expanded lattice (Chern number $= \pm 1$) and the shrunk lattice (Chern number $= 0$), a pair of interface states appears inside the band gap located at the domain interface [12]. The interface modes are protected by pseudo-time-reversal symmetry, and they propagate in opposite directions along the interface, where the chirality of the Poynting vector is linked with the momentum along the edge. We made adjacently placed shrunk and expanded hexagonal photonic lattices as schematically shown in Fig. 4(a); the corresponding SEM image is shown in Fig. 4(b).

We performed angle-resolved CL with the electron beam positioned at the edge. We found results quite similar to those for bulk lattice states probed one or more lattice units away from the edge. We attribute this to the fact that CL probes extended lattice states, as shown also by the band structure measurements in Fig. 3, and therefore CL cannot sensitively probe just the edge states alone. Confocal optical transmission spectroscopy was then performed using an unpolarized light beam from a halogen lamp that was weakly focused onto the sample. The transmitted light

either in the bulk shrunk or expanded regions or centered at the interface [Fig. 4(d)] was collected with $\sim$600 nm spatial resolution using a confocal microscope with a 50x objective. For the bulk expanded and shrunk regions a clear band gap around 640 nm is observed in the transmission spectrum, with sharp dips corresponding to the band edges. For the edge region, a single deep minimum is observed, slightly shifted from the higher band edge, consistent with the existence of an interface state. For the shrunk lattice, the strongest coupling (largest transmission dip) is observed for the low-energy band, consistent with the (bright) dipolar nature of this band [12]. The smaller coupling to the (dark)
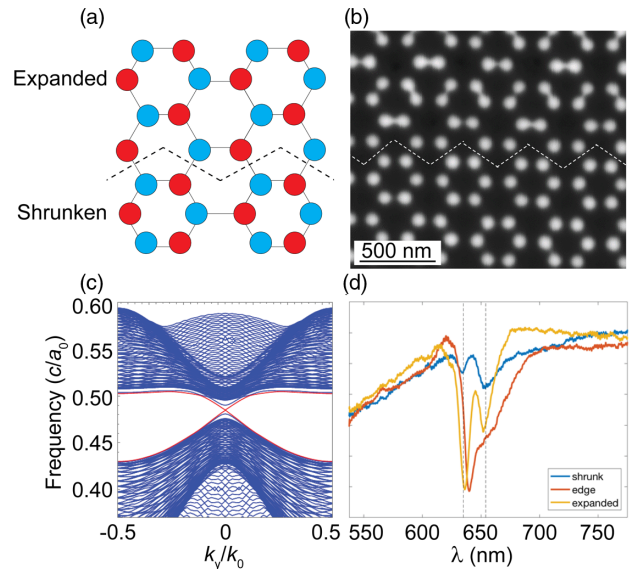


FIG. 4. Edge states between shrunk and expanded hexagonal photonic lattices. (a) Edge geometry. (b) SEM image of edge region. (c) Numerically calculated band structure, red lines indicate edge states. (d) Optical transmission spectra taken in bulk and edge regions, black dashed lines indicate the band gap.

quadrupolar band is also observed and is attributed to the finite angular range (numerical aperture NA = 0.2) used in the measurements. In contrast, for the expanded lattice the strongest coupling is observed for the high-energy band, directly reflecting the band inversion in this geometry.

In summary, we have designed and fabricated two-dimensional hexagonal photonic lattices of silicon Mie resonators that possess topological band structure in the visible spectral range. Conventional hexagonal lattices show a double-conical Dirac band structure with the Dirac point at 450–650 nm, depending on the geometry. By slightly shrinking or expanding the hexagonal unit cell, we form hexagonal superstructures for which a band gap opens and the double-degenerate Dirac bands split. Good agreement is observed between measurements and numerical simulations. Coherent 30 keV electron beam excitation proves a powerful tool to probe the radiative local density of optical states and the dispersion of topological lattices. Using optical scattering, we confirm the existence of interface states between shrunk and topological lattices which, according to theory, are topologically protected against coupling between counterpropagating modes. This work demonstrates the feasibility to realize practical silicon-based topological geometries that are commensurate with planar Si-based integrated optics technology, and to excite them locally with electron beams.

---

[*]Corresponding author.
A.Polman@amolf.nl

[1] S. Raghu and F. D. M. Haldane, Analogs of quantum-Hall-effect edge states in photonic crystals, Phys. Rev. A **78,** 033834 (2008).

[2] L. Lu, J. D. Joannopoulos, and M. Soljačić, Topological photonics, Nat. Photonics **8,** 821 (2014).

[3] A. B. Khanikaev, S. Hossein Mousavi, W.-K. Tse, M. Kargarian, A. H. MacDonald, and G. Shvets, Photonic topological insulators, Nat. Mater. **12,** 233 (2013).

[4] A. Blanco-Redondo, I. Andonegui, M. J. Collins, G. Harari, Y. Lumer, M. C. Rechtsman, B. J. Eggleton, and M. Segev, Topological Optical Waveguiding in Silicon and the Transition between Topological and Trivial Defect States, Phys. Rev. Lett. **116,** 163901 (2016).

[5] D. Leykam, M. C. Rechtsman, and Y. D. Chong, Anomalous Topological Phases and Unpaired Dirac Cones in Photonic Floquet Topological Insulators, Phys. Rev. Lett. **117,** 013902 (2016).

[6] Z. Wang, Y. Chong, J. D. Joannopoulos, and M. Soljačić, Observation of unidirectional backscattering-immune topological electromagnetic states, Nature (London) **461,** 772 (2009).

[7] M. C. Rechtsman, J. M. Zeuner, Y. Plotnik, Y. Lumer, D. Podolsky, F. Dreisow, S. Nolte, M. Segev, and A. Szameit, Photonic Floquet topological insulators, Nature (London) **496,** 196 (2013).

[8] M. Hafezi, S. Mittal, J. Fan, A. Migdall, and J. M. Taylor, Imaging topological edge states in silicon photonics, Nat. Photonics **7,** 1001 (2013).

[9] L. Lu, Z. Wang, D. Ye, L. Ran, L. Fu, J. D. Joannopoulos, and M. Soljačić, Experimental observation of Weyl points, Science **349,** 622 (2015).

[10] S. Barik, A. Karasahin, C. Flower, T. Cai, H. Miyake, W. DeGottardi, M. Hafezi, and E. Waks, A topological quantum optics interface, Science **359,** 666 (2018).

[11] T. Ma and G. Shvets, All-Si valley-Hall photonic topological insulator, New J. Phys. **18,** 025012 (2016).

[12] L.-H. Wu and X. Hu, Scheme for Achieving a Topological Photonic Crystal by Using Dielectric Material, Phys. Rev. Lett. **114,** 223901 (2015).

[13] G. Siroki, P. A. Huidobro, and V. Giannini, Topological photonics: From crystals to particles, Phys. Rev. B **96,** 041408 (2017).

[14] M. A. Gorlach, X. Ni, D. A. Smirnova, D. Korobkin, D. Zhirihin, A. P. Slobozhanyuk, P. A. Belov, A. Alù, and A. B. Khanikaev, Far-field probing of leaky topological states in all-dielectric metasurfaces, Nat. Commun. **9,** 909 (2018).

[15] See Supplemental Material at http://link.aps.org/supplemental/10.1103/PhysRevLett.122.117401 further details on sample fabrication, numerical simulations of band structure dispersion, cathodoluminescence and confocal microscopy measurements.

[16] W. Chang, C. P. Kao, G. A. Pike, J. A. Slone, and E. Yablonovitch, Vapor phase epitaxial liftoff of GaAs and silicon single crystal films, Sol. Energy Mater. Sol. Cells **58,** 141 (1999).

[17] A. Tilke, M. Rotter, R. H. Blick, H. Lorenz, and J. P. Kotthaus, Vapor phase epitaxial liftoff of GaAs and silicon single crystal films, Appl. Phys. Lett. **77,** 558 (2000).

[18] M. Cho, J.-H. Seo, J. Lee, D. Zhao, H. Mi, X. Yin, M. Kim, X. Wang, W. Zhou, and Z. Ma, Ultra-thin distributed Bragg reflectors via stacked single-crystal silicon nanomembranes, Appl. Phys. Lett. **106,** 181107 (2015).

[19] R. Sapienza, T. Coenen, J. Renger, M. Kuttge, N. F. van Hulst, and A. Polman, Deep-subwavelength imaging of the modal dispersion of light, Nat. Mater. **11**, 781 (2012).

[20] B. J. M. Brenny, A. Polman, and F. J. García de Abajo, Femtosecond plasmon and photon wave packets excited by a high-energy electron on a metal or dielectric surface, Phys. Rev. B **94**, 155412 (2016).

[21] F. J. García de Abajo, Optical excitations in electron microscopy, Rev. Mod. Phys. **82**, 209 (2010).

[22] Y. Yang, A. Massuda, C. Roques-Carmes, S. E. Kooi, T. Christensen, S. G. Johnson, J. D. Joannopoulos, O. D. Miller, I. Kaminer, and M. Soljačić, Maximal spontaneous photon emission and energy loss from free electrons, Nat. Phys. **14**, 967 (2018).

[23] S. Mignuzzi, M. Mota, T. Coenen, Y. Li, A. P. Mihai, P. K. Petrov, R. F. M. Oulton, S. A. Maier, and R. Sapienza, Energy-momentum cathodoluminescence spectroscopy of dielectric nanostructures, ACS Photonics **5**, 1381 (2018).

[24] T. Coenen, J. van de Groep, and A. Polman, Resonant modes of single silicon nanocavities excited by electron irradiation, ACS Nano **7**, 1689 (2013).

[25] J. van de Groep and A. Polman, Designing dielectric resonators on substrates: Combining magnetic and electric resonances, Opt. Express **21**, 26285 (2013).

[26] T. Coenen, F. Bernal Arango, A. Femius Koenderink, and A. Polman, Directional emission from a single plasmonic scatterer, Nat. Commun. **5**, 3250 (2014).

[27] J. van de Groep, T. Coenen, S. A. Mann, and A. Polman, Direct imaging of hybridized eigenmodes in coupled silicon nanoparticles, Optica **3**, 93 (2016).

[28] L. Langguth, D. Punj, J. Wenger, and A. F. Koenderink, Plasmonic band structure controls single-molecule fluorescence, ACS Nano **7**, 8840 (2013).

[29] D. E. Aspnes and A. A. Studna, Dielectric functions and optical parameters of Si, Ge, GaP, GaAs, GaSb, InP, InAs, and InSb from 1.5 to 6.0 eV, Phys. Rev. B **27**, 985 (1983).